ESTIMATION OF CRUSTAL MOVEMENT IN THE 2016 KUMAMOTO, JAPAN, EARTHQUAKE BY RELATIVE GNSS POSITIONING WITH LONG BASELINE

Kei Nakanishi[1], Wen Liu[1] and Fumio Yamazaki[1]
[1]Chiba University, 1-33, Yayoi-cho, Inage-ku, Chiba, 263-8522, Japan.
acca2156@chiba-u.jp; wen.liu@chiba-u.jp; fumio.yamazaki@faculty.chiba-u.jp

KEY WORDS: GEONET, long baseline, the 2016 Kumamoto earthquake, crustal movement, standard deviation

ABSTRACT: In this study, an accurate estimation of the crustal movement in the 2016 Kumamoto earthquake was attempted based on the relative GNSS positioning method with reference to 113 GEONET sites in Japan. Those GEONET sites were located from 100 km to 1,200 km away the epicenter. In order to evaluate the variations of permanent displacements in terms of baseline distance, the different stations were set as the base station. We processed the coordinate of the GEONET Kumamoto station, which is located approximately 5-km north from the epicenters of the M_{JMA} 6.5 and M_{JMA} 7.3 earthquakes, by the relative GNSS positioning in the period of April 14-17, 2016. The relationship between the performance of displacements and baseline distance was investigated. As a result, the range of 200-400 km baseline length achieved the most accurate measurement and the displacement distribution in this range was estimated using the GEONET Kumamoto station as the rover station.

1. INTRODUCTION

The distribution of crustal movements is important for early warning systems because it can be used to estimate earthquake source parameters and to stimulate tsunami propagation (Ohta et al., 2016). Many studies have been conducted to estimate the crustal movement in the 2016 Kumamoto, Japan, earthquake. There are mainly three techniques: from acceleration records (Fujiwara et al., 2016), from satellite Synthetic Aperture Radar (SAR) data (Ronni et al., 2017) and from Global Navigation Satellite System (GNSS) network data (Kawamoto et al., 2016). Recently, other new methods are utilized to estimate crustal movements, such as Lidar data (Moya et al., 2017a). The airborne Lidar technology is an integrated system consisting of a GNSS, an inertial navigation system (INS), and a laser scanner. The crustal movement estimated from the double integration of the acceleration records shows significant errors produced by zero line shift (Boore, 2001). Lidar and SAR data enable to grasp crustal movements and damage situations for a wide range continuously. On the other hand, these methods require more than two images. Thus, the displacements from them have a low temporal resolution. From GNSS networks, real-time and accurate estimation of crustal movements is possible based on the relative GNSS positioning.

The relative GNSS positioning is a precise positioning technique. Users can obtain the cm-level accuracy of positions by the measurement of GNSS signals received at an unknown station (rover station) and a station with known coordinates that must remain constant in time (master station). The vector between the two stations is known as the baseline (BL) vector. In order to perform high accuracy positioning, the baseline is desirable to be less than 10-20 km (Sagiya, 2004). However, the short baseline (less than 10-20 km) method is not useful to estimate a co-seismic crustal movement because the seismic ground motion spreads widely and the master station shakes during the earthquake. Therefore, the relative positioning with a long baseline (a master station far from the epicenter) is effective to estimate co-seismic crustal movements (Moya et al., 2017b).

With a longer BL over 100 km, however, the relative positioning faces many difficulties compared to the short BL method. The differences of the atmospheric effects, such as the broadcast ephemeris, the ionosphere, the troposphere and the earth tides effects, between the rover and master stations become enormous and cannot be negligible. The method to solve these differences can be divided broadly into two methods, depending on the distance of the BL length. The first method is used for short BL lengths. In this method, the atmospheric effects for the reference and master stations are considered as equal, thus the differences are eliminated by the double phase difference described later. The second method is used for the case of long BL lengths. It establishes approximate equations of the atmospheric effects and deleting the differences by taking the difference of the equations from the relative positioning solution. The former is called “the short BL method” and the latter “the long BL method”. The short BL method can achieve centimeter-level accuracy for the BL distance less than 20 km although errors increase as the BL increases (Takasu and Yasuda, 2010). Another effective utilization of the long BL relative positioning method is the case that a rover station locates on the sea, for example the tsunami monitoring system developed in Japan (Kato et al., 2001). We hardly can search a fixed and stable master station on the sea, except for that settled on the ground nearby the coast. The tsunami system consists of GNSS-equipped buoys and can find coming tsunami by buoys and transmit

GNSS observation data to the master station. These buoys are currently only within approximately 15-km away from the coast because of the limitation of the baseline length. If the long BL relative positioning method is used, the range for tsunami detection will expand.

In this study, the detection of crustal movement in the 2016 Kumamoto, Japan, earthquake is attempted based on the relative positioning method with reference to 113 GEONET sites, which are located from 50 km to 1,200 km away the epicenter. Then, the relationship between the performance of displacements and BL length is investigated. Moreover, the relationship between the shaking intensity and the positioning accuracy is estimated.

2. CARRIER PHASE RELATIVE POSITIONING

2.1 Carrier Phase and Pseudo-range Observation

The signal transmitted from the GPS satellites consists of both the code and carrier phase including two frequencies, L1 at 1575.42 MHz and L2 at 1227.60 MHz, as shown in **Figure 1**. The L1 signal is modulated with both of the Precision (P) code and the Coarse Acquisition (C/A) code. The P code is a long precision code operating at 10.23 Mbps and the C/A code is a short code operating at 1.023 Mbps. The L2 signal is modulated with the P code only. The P and C/A codes have the unique patterns for each satellite, which are called the Pseudo-Random Noise (PRN) codes. The function of the PRN codes is, firstly, the identification of satellites by judging which code pattern is matched with a like code generated in the receiver. Secondary, it can measure the navigation-signal transit time by calculating the phase shift required to match the transmitted code with the generated code in the receiver (Milliken and Zoller, 1978). Thus, the geometric distance between the satellite j and the observation point i ($\rho_i^j(\mathrm{t})$) can be obtained from the codes. The navigation signal transit time ($t_i - t^j$) is used to calculate it according to Eq. (1), where c is the propagation speed of electromagnetic waves in space.

$$\rho_i^j(t) = c(t_i - t^j) \tag{1}$$

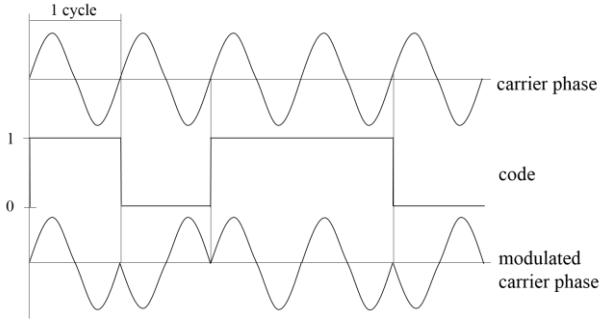

Figure 1. Biphase modulation of the carrier phase of GPS signal

The carrier phase and pseudo-range are calculated in a receiver using the geometric distance, atmospheric delay, satellite's and receiver's time error. The single positioning only uses the pseudo-range to detect the user's position, so it can be calculated by one receiver. On the other hand, the relative positioning aims to calculate the vector between a rover station and a master station, so it needs two stations. The carrier phase and pseudo-range observation models for the master station (point A) and the rover station (point B) for a given satellite j at time t are given by:

$$\begin{aligned}
\Phi_A^j(\mathrm{t}) &= \frac{1}{\lambda}\left[\rho_A^j(t) - I_A^j(t) + T_A^j(t)\right] + f(\delta t_A - \delta t^j) + N_A^j + \varepsilon_{\Phi,A}^j \\
\Phi_B^j(\mathrm{t}) &= \frac{1}{\lambda}\left[\rho_B^j(t) - I_B^j(t) + T_B^j(t)\right] + f(\delta t_B - \delta t^j) + N_B^j + \varepsilon_{\Phi,B}^j \\
\mathrm{P}_A^j(\mathrm{t}) &= \rho_A^j(t) - I_A^j(t) + T_A^j(t) + c(\delta t_A - \delta t^j) + \varepsilon_{P,A}^j \\
\mathrm{P}_B^j(\mathrm{t}) &= \rho_B^j(t) - I_B^j(t) + T_B^j(t) + c(\delta t_B - \delta t^j) + \varepsilon_{P,B}^j
\end{aligned} \tag{2}$$

where $\Phi_i^j(t)$ is the carrier phase measurement expressed in cycles, $P_i^j(t)$ is the pseudo-range expressed in units of meters, λ is the carrier wavelength and f is the carrier frequency. $\rho_i^j(\mathrm{t})$ is the geometric distance between the satellite j and the observed point i, $I_i^j(t)$ is the ionospheric advance, $T_i^j(t)$ is the tropospheric delay, which are all expressed in units of meters. δt_i and $\delta \mathrm{t}^j$ are the antenna and satellite clock biases, respectively, which are expressed in units of seconds. N_i^j is the integer carrier phase cycle ambiguity, which is the total number of full cycles between the satellite j and the observed point i. ε is the carrier phase measurement error due to receiver noise and multipath.

2.2 Single and Double Difference

The single differences of Eq. (2) are formed by subtracting the master station's observed equation from the rover station's to cancel the unknown terms.

$$\begin{aligned} \Phi_{AB}^{j}(\mathrm{t}) &= \frac{1}{\lambda}\left[\rho_{AB}^{j}(t) - I_{AB}^{j}(t) + T_{AB}^{j}(t)\right] + f\delta t_{AB} + N_{AB}^{j} + \varepsilon_{\Phi,AB}^{j} \\ \mathrm{P}_{AB}^{j}(\mathrm{t}) &= \rho_{AB}^{j}(t) - I_{AB}^{j}(t) + T_{AB}^{j}(t) + c\delta t_{AB} + \varepsilon_{P,AB}^{j} \end{aligned} \tag{3}$$

which follows the symbolic equation that is also used later:

$$\begin{aligned} *_{AB}^{j} &= *_{B}^{j} - *_{A}^{j} \\ *_{AB}^{jk} &= *_{AB}^{k} - *_{AB}^{j} \end{aligned} \tag{4}$$

In Eq. (3), the satellite clock bias ($\delta \mathrm{t}^{j}$) term has cancelled out of the single difference equation. Furthermore, the ionosphere advance ($I_i^j(t)$) and the troposphere delay ($T_i^j(t)$) are canceled in Eq. (3) when the BL is short, because they are assumed to be equal for both the master and rover stations as shown in **Figure 2.** When the BL is relatively long (approximately 10 - 100 km), the ionosphere advances ($I_i^j(t)$) are hard to be eliminated by the double differences. In this case, dual-frequency measurements (Liu, 2010; Brunini, 2010) are often used to eliminate the ionosphere effects. With a longer BL over 100 km, the error terms in Eq. (3) caused by the broadcast ephemeris errors, troposphere delay and earth tides effects cannot be negligible. It is useful to model the error terms in the measurement equation, such as the Slant Total Electron Content (STEC) for the ionosphere advance (Ciraolo et al., 2007), and the Zenith Total Delay (ZTD) observation model (Blewitt, 1989) or the Saastamoinen model for the troposphere delay (Teunissen, 1995). We can subtract the ionosphere advance ($I_i^j(t)$) and the troposphere delay ($T_i^j(t)$) in Eq. (3) using these models. The final forms of the single difference equation become:

$$\begin{aligned} \Phi_{AB}^{j}(\mathrm{t}) &= \frac{1}{\lambda}\rho_{AB}^{j}(t) + f\delta t_{AB} + N_{AB}^{j} + \varepsilon_{\Phi,AB}^{j} \\ \mathrm{P}_{AB}^{j}(\mathrm{t}) &= \rho_{AB}^{j}(t) + c\delta t_{AB} + \varepsilon_{P,AB}^{j} \end{aligned} \tag{5}$$

There are still two unknown terms: the integer ambiguity (N_i^j) and the antenna clock bias (δt_i). We can use a double difference if there are two satellites

$$\begin{aligned} \Phi_{AB}^{jk}(\mathrm{t}) &= \frac{1}{\lambda}\rho_{AB}^{jk}(t) + N_{AB}^{jk} + \varepsilon_{\Phi,AB}^{jk} \\ \mathrm{P}_{AB}^{jk}(\mathrm{t}) &= \rho_{AB}^{jk}(t) + \varepsilon_{P,AB}^{jk} \end{aligned} \tag{6}$$

In Eq. (6), the antenna clock bias term has cancelled out of the double difference equation. Double difference needs at least three sets of twin satellites. It can be realized using at least four satellites.

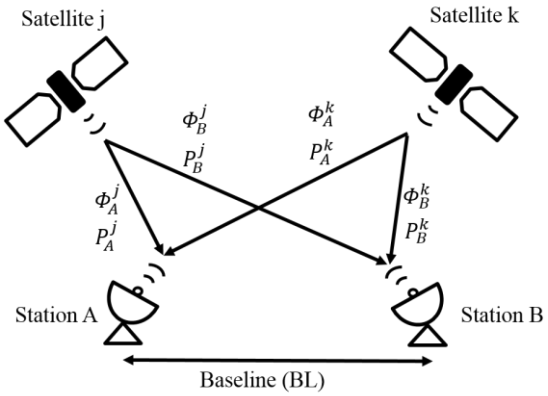

Figure 2. Principal of the relative positioning method

2.3 Integer Ambiguity Resolution

The integer Ambiguity Resolution (AR) is a key technique to obtain precise solutions. Many techniques are useful to resolve this problem, such as the utilization of change of multiple solutions corresponding to the movement of satellites. It is possible to obtain very precise AR by observing satellites as long as possible in time, combining as many satellites as possible or utilizing the linear combination (LC) of L1 and L2 codes. For a short BL, the original observables L1 and L2 carrier phases and P code are used to obtain solutions. Since many efficient and reliable algorithms as AR techniques, such as LAMBDA (Teunissen et al., 1997), have been developed recently, we employ LAMBDA in this study. After the integer AR, a true positioning solution can be obtained, and it is called "fix resolution". The ratio of the "fix resolution" out of all solutions is called "the fix ratio". Thus, higher the fix ratio is, the positioning accuracy becomes better.

3. GEONET

The GEONET (GNSS Earth Observation Network System) is the GNSS station network of Japan developed by the Geospatial Information Authority (GSI) of Japan (2016). The system has more than 1,300 GNSS receiving stations covering Japan's territory uniformly, A typical GEONET station consists of a 5-m tall stainless pillar equipped with a dual-frequency GPS receiver, a GPS antenna, and a modem connected to a digital telephone line (ISDN). All the GEONET stations enable to transmit an epoch-by-epoch data so as to be utilized for real-time monitoring of crustal movement and other purposes. The 1-Hz sampling data are transmitted to the GEONET control center in the GSI headquarters on a real-time basis and they are stored temporarily.

As one of its application, the co-seismic and post-seismic crustal movements have been measured using continuous fixed points observation for many earthquakes since 1994 including the 2016 Kumamoto earthquake. The calculation of displacements in high accuracy can be performed by the relative positioning method using a pair of GEONET stations as the rover and master. The GEONET is also used to monitor long-term crustal movements, and to detect volcanic activities. The GEONET data have also been used in other research areas such as geodesy, ionospheric research and so on.

4. A CASE STUDY

4.1 The Kumamoto Earthquake Sequence

The 2016 Kumamoto earthquake sequence started with a M_{JMA} 6.5 earthquake at 21:26 (JST) on April 14, 2016. The epicenter was located at the end of the Hinagu fault with a shallow depth as shown in **Figure 3**. A larger earthquake of M_{JMA} 7.3 occurred at 01:25 (JST) on April 16, 2016, approximately 28 hours after the M_{JMA} 6.5 earthquake. The epicenter was located at the Futagawa fault, which is closely located the Hinagu fault. Thus the M_{JMA} 6.5 event was designated as the foreshock and the M_{JMA} 7.3 event as the main-shock. The epicenters of the both events were located in Mashiki town (about 33 thousand-population), in the east of Kumamoto city (about 735 thousand-population). The total number of aftershocks (larger than magnitude 3.5) reached 340 times as of April 30, 2017, one year after the foreshock. This number is the largest among recent inland (crustal) earthquakes in Japan (Japan Meteorological Agency, 2016).

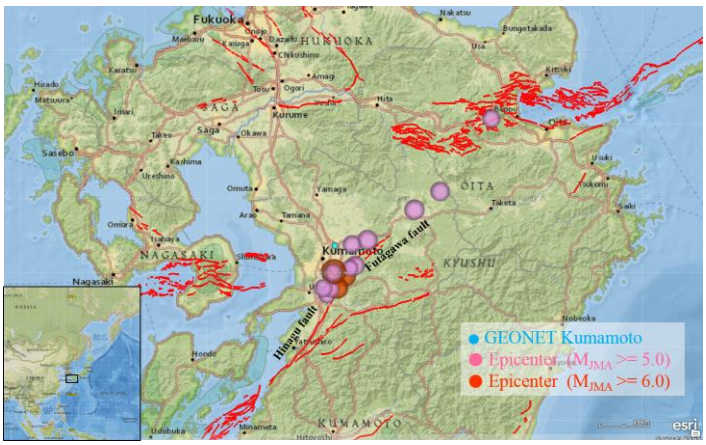

Figure 3. The affected area of the Kumamoto earthquake and the locations of the GEONET Kumamoto station, and the epicenters of the earthquake sequence in the period of April 14 - 17, 2016 ($M_{JMA} \geq 5.0$).

The displacement of 75 cm to the east-northeast (ENE) was observed at the Kumamoto station while that of 97 cm to the southwest (SE) was recorded at the Choyo station during the main-shock. These observations validated the right-lateral strike-slip mechanism of the Futagawa fault.

4.2 Method

In this study, GEONET observation data provided by GSI (http://www.gsi.go.jp/ENGLISH/index.html) were used. The used data were recorded in the period of April 14-17, 2016, including the main-shock, the foreshock and many aftershocks. They are in the Receiver Independent Exchange Format (RINEX) data with 30-s intervals, and a data processing becomes possible by using the open source package RTKLIB (http://www.rtklib.com) for GNSS positioning. In case of the relative positioning processing, setting of the rover station and the master station is required. We set up the GEONET Kumamoto station, which is located approximately 5-km north from the epicenters of the foreshock and main-shock, as the rover station as shown in **Figure 3**.

As the master station, we used a total of 113 GEONET stations, approximately 50 - 1200 km away from the Kumamoto station, as shown in **Figure 4 (a)** by red points. The reason why we selected the master station with different distances in spite of setting the same rover station is to examine the effects of the BL distance in the result of the rover station's positioning. Then the range for realizing the appropriate positioning for the long BL method can be determined.

In addition, the relationship between the JMA instrumental seismic intensity (indicating the strength of shaking; Shabestari and Yamazaki, 2001; Karim and Yamazaki, 2002) and the positioning accuracy was investigated considering the utilization of the current method during an earthquake. The JMA seismic intensities observed by the foreshock were much smaller than those by the main-shock as shown in **Figure 4**. But even for the foreshock, the area of JMA Intensity 1 (the shaking level such that people in a quiet indoor place can recognize it) exceeded a 200-km radius from the epicenter. Whether earthquake shaking affects positioning accuracy or not seems to be necessary to investigate for the long BL positioning. Here the seismic intensity data were provided from J-RiSQ (www.j-risq.bosai.go.jp/report/).

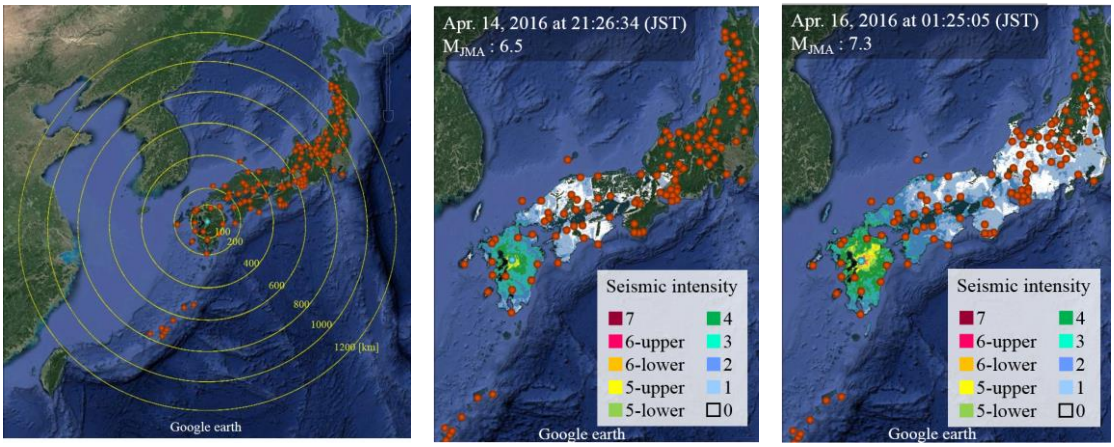

(a) (b) (c)

Figure 4. (a) Location of the master stations (red points) and the distance from the GEONET Kumamoto station (yellow circles). Distribution of the JMA seismic intensity for the April 14 (b) and 16 (c) events.

Table 1 Option setting for the long BL method

Option	Setting		
Positioning mode	Kinematic	Min elevation to fix ambiguity	25°
Frequencies	L1+L2	Min elevation to hold ambiguity	35°
Receiver dynamics	OFF	Code/Carrier-phase error ratio: L1, L2	1000, 100
Earth tides correction	ON	Carrier phase error	0.003+0.003/sin ele (m)
Elevation mask	10°	Satellite antenna model	IGS08.ATX
Ionosphere correction	Estimate STEC	Receiver antenna model	IGS08.ATX
Troposphere correction	Estimate ZTD + Gradient	Process noise of vertical ionosphere. delay	10^{-3} m/sqrt (s)
Satellite ephemeris	Precise	Process noise of zenith tropos delay	10^{-4} m/sqrt (s)

For the relative positioning with long BL lengths, the parameters for correcting atmospheric and satellite ephemeris errors must be used. The details of option setting for the long BL method are shown in **Table 1**. The AR method, ionosphere correction and troposphere correction were carried out based on those built in RTKLIB. The ultra-rapid product of the ephemerides offered in near real-time by the International GNSS Service (IGS) (www.igs.org/). A complete description of the method can found in Takasu and Yasuda (2010).

5. RESULTS

Figure 5 shows the results of the relative positioning by the long BL method from April 14 to 17 in 2016, for all the GEONET stations used in this study. In the figure, the standard deviation and the fix ratio are plotted as a function of the distance from the GEONET Kumamoto station to each master GEONET station. The color of the marks shows the JMA seismic intensity of the master station in the main-shock. In **Figure 5 (a)**, the standard deviations of all the three components is seen to increase as the BL distance increases, and the standard deviation is especially large for the UD component. As a whole, the effects of the seismic intensity to the standard deviation looks not so large.

Figure 5 (b) shows the fix ratio for all the stations. Similar to the standard deviation, the fix ratio also deteriorates as the BL distance increases. Focusing on the influence of the seismic intensity, highly accurate fix ratios can be seen even at the points of seismic intensities 4 or 5-upper. Thus, the seismic intensity is considered not to affect the accuracy so much. However, at the points of the seismic intensity 3, some low fix ratio results are included. On the other hand, there is no point where the fix rate deteriorates in the range of 200 - 400 km, and it can be said that the positioning is accurately performed at all the points.

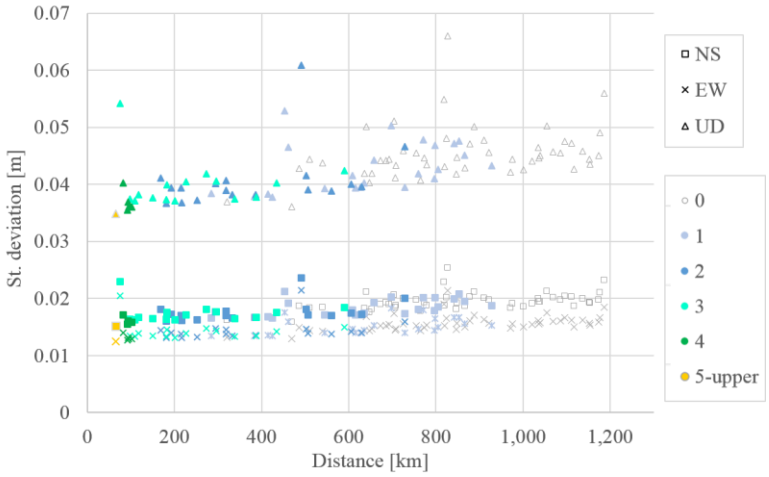

(a)

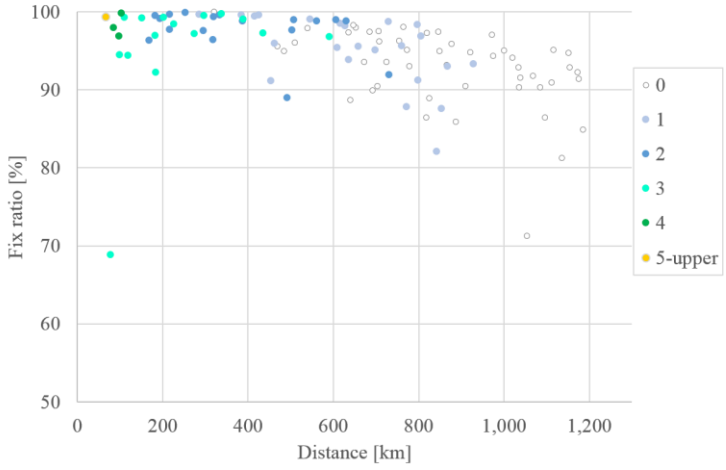

(b)

Figure 5. Relationship between the BL distance and standard deviation (a) and fix ratio (b) for different JMA seismic intensity scale points.

Table 2. Accuracy evaluation based on fix ratio and standard deviation, classified by the BL distances

		BL distance [km]						
		50-100	100-200	200-300	300-400	400-500	500-600	600-700
Fix ratio	More than 95%	5/7	7/9	9/9	8/8	5/8	7/8	11/15
	More than 99%	2/7	5/9	6/9	5/8	1/8	1/8	0/15
St. dev	Less than 4.5 [cm]	5/7	6/9	4/9	6/8	2/8	3/8	0/15

700-800	800-900	900-1000	1000-1100	1100-1200	total
8/14	4/13	1/5	1/9	1/8	67/113
0/14	0/13	0/5	0/9	0/8	20/113
0/14	0/13	0/5	0/9	0/8	26/113

Table 2 shows the number of the master stations with the fix ratio larger than 95 % and 99 %. The standard deviation was obtained by the square root of the sum of the three components' variances. **Table 2** also shows the number of the master stations where the standard deviation was less than 4.5 cm. As shown in the results, the fix ratio was more than 95 % for all the stations in the range of 200-400 km, and over 99 % for more than half stations. It represents the positioning could be performed precisely and stably even for long BL distances. The standard deviations were less than 4.5 cm in this range. The standard deviation is generally influenced by the distance, but highly accurate positioning results were obtained in this study.

When the BL distance was longer than 400 km, there was almost no station whose the fix ratio more than 99 %. It indicates the positioning performed unsteadily. Furthermore, the standard deviation for most of the stations were larger than 4.5 cm. It represents the accuracy of the results obtained by positioning was low. Although those stations hardly affected by earthquake shaking because of the long epicentral distance, their uses were low in this situation. A processing method to improve the positioning accuracy is required.

The seismic motion was large at many stations in the range of 50-200 km BL distance, but only a few stations were affected by the strong shaking. Furthermore, the standard deviation shows good values compared with those of the longer BL distance than 200 km. At a first glance, it seems worthy to calculate crustal deformation using these data at the time of an earthquake. But, in the range of 50 - 200 km, there were at least several stations affected by the earthquake, and it is difficult to identify such stations immediately. A possibility of selecting a master station that produces low positioning accuracy becomes higher than those in the range of 200-400 km. For this reason, the stations within this range are considered inappropriate as the master station used for calculating crustal deformation soon after the occurrence of an earthquake.

Figure 6 shows the positioning results of the GEONET Kumamoto station in the period of April 14-17 in 2016. In the figure, the GEONET Tsuki (BL: 82.98 km), the Toyomatsu (320.67 km), and the Iide (1,000.87 km) stations were used as the master stations, respectively. The green point in the figure represents a fix solution and the orange point indicates a solution, in which the AR was not determined as an accurate integer value. Accurate positioning was considered to be carried out at the green points.

The fix solution was obtained at the most of time for the 50-200 km BL distance in spite of the large magnitude events occurred (**Table 3),** as shown in **Figure 6 (a)**. The strong shaking affected only a little. However, in the period when the fix solution was not obtained, there were large errors of approximately 20 cm to the EW, NS and UD directions. This is considered to be caused by the fact that the equation of the atmospheric model used in the analysis was largely deviated from the actual value for the long BL of a comparatively short distance.

The fix solutions were obtained in almost all the time zones when the BL is in the 200-400 km distance range, as shown in **Figure 6 (b)**. The fix solutions wee continuously obtained even at the time when a large earthquake occurred. On the contrary, the fix solutions could not be obtained frequently when the BL distance was over 400 km, as shown in **Figure 6 (c)**. Furthermore, there was remarkable deterioration in accuracy when the large shaking occurred. These three cases are just examples in each BL range, but similar trends were observed in each range's other base stations. Especially in the range of 200-400 km BL distance, the fix positioning solutions could be obtained in almost all the time zones at all the stations.

Table 3. Log of the Kumamoto earthquake during April 14 - 17, 2016 ($M_{JMA} \geq 6.0$) by JMA.

No.	Date & Time (JST)	M_{JMA}	Latitude	Longitude	Depth [km]
1	Apr. 14, 2016 at 21:26:34	6.5	32° 44.5′ N	130° 48.5′ E	11
2	Apr. 15, 2016 at 00:03:46	6.4	32° 42.0′ N	130° 46.6′ E	7
3	Apr. 16, 2016 at 01:25:05	7.3	32° 45.2′ N	130° 45.7′ E	12

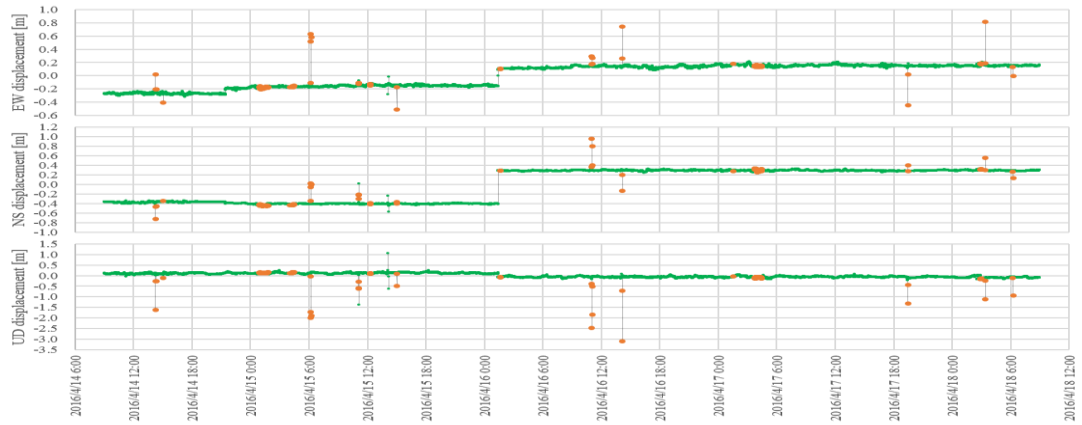

(a)

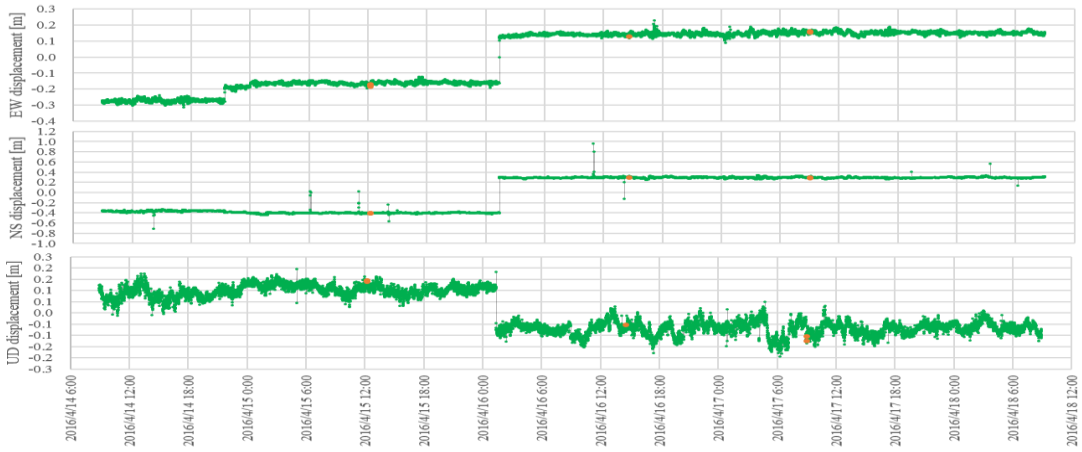

(b)

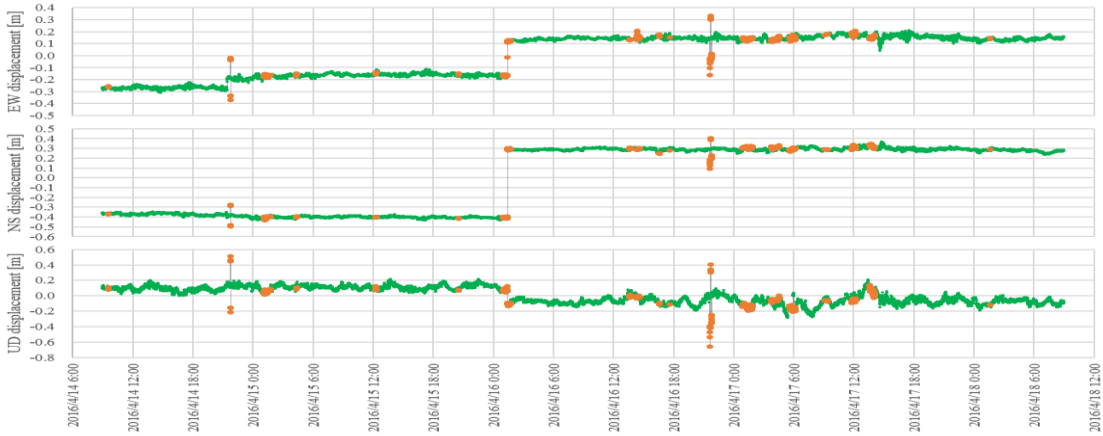

(c)

Figure 6. Displacement of the GEONET Kumamoto station when (a) Tsuki (BL: 82.98 km), (b) Toyomatsu (320.67 km) and (c) Iide (1,000.87 km) stations were set as the reference station, respectively.

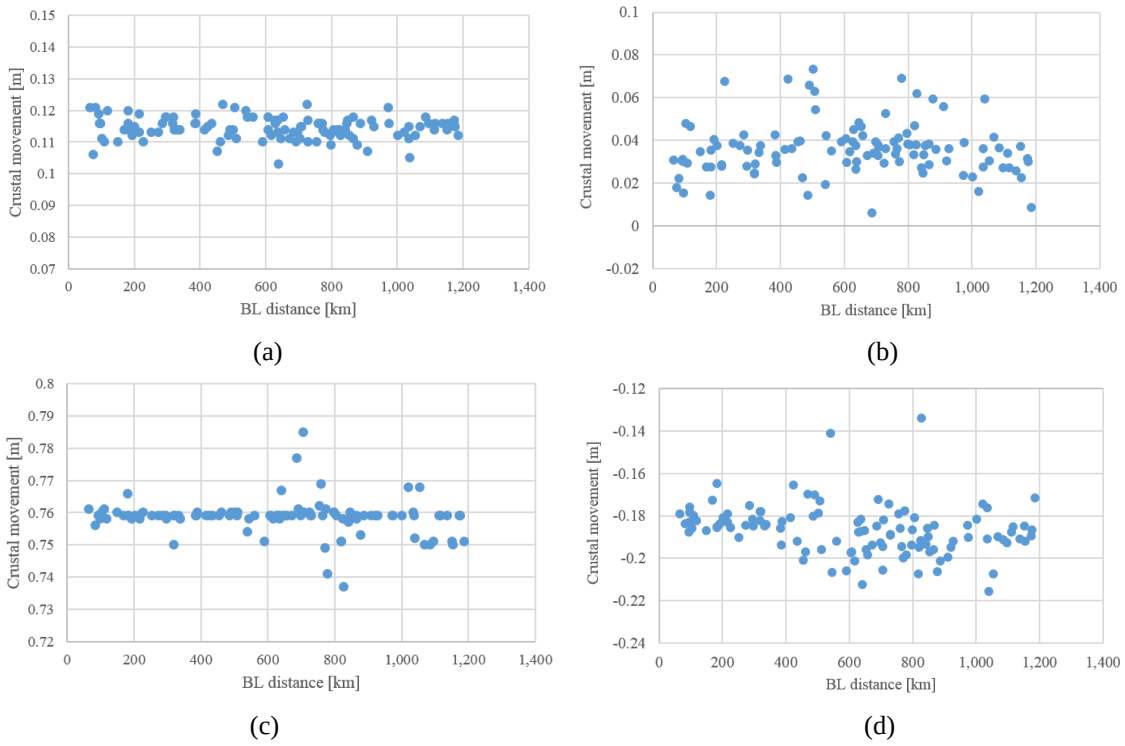

Figure7. Relationship between the BL distance and crustal movement due to the M_{JMA}6.5 earthquake on April 14, 2016 and the M_{JMA}6.4 earthquake on April 15 to the horizontal (a) and vertical (b) directions; the one due to the M_{JMA}7.3 earthquake on April 16, 2016 to the horizontal (c) and vertical (d) directions.

In addition, the displacements at the GEONET Kumamoto station to the NS, EW, and UD directions were obtained by referring to 113 GEONET stations selected in this study as the master stations. The displacements due to the three large magnitude earthquakes shown in **Table 3** were calculated. First, the average values of the coordinates of the GEONET Kumamoto station before the M_{JMA}6.5 earthquake, and the one from the M_{JMA} 6.4 earthquake to the M_{JMA}7.3 earthquake were calculated. Then, the magnitude of crustal deformation by the M_{JMA}6.5 and M_{JMA} 6.4 earthquakes calculated by subtracting these two values as shown in **Figure 7 (a-b).** Similarly, the crustal movement due to the M_{JMA}7.3 earthquake was obtained by subtracting the average value of the coordinates before and after the M_{JMA}7.3 earthquake, as shown in **Figure 7 (c-d)**.

As mentioned above, the relative positioning using the master stations in the range of 200-400 km BL distance was most reliable. Considering that, the most accurate crustal movement at the GEONET Kumamoto station was 11 - 12 cm in the horizontal and +2 - 4 cm in the vertical directions for the M_{JMA}6.5 event on April 14, 2016 and the M_{JMA}6.4 on April 15, whereas approximately 76 cm in the horizontal and -19 - 18 cm in the vertical directions for the M_{JMA}7.3 event on April 16, 2016. The Geospatial Information Authority of Japan (2016) reported the crustal movement of the GEONET Kumamoto station with reference to the GEONET Misumi station (BL: 296.36 km) as the master station. According to it, the crustal movement of the GEONET Kumamoto station was 12 cm in the horizontal and +4 cm in the vertical directions for the M_{JMA}6.5 and M_{JMA}6.4 earthquakes, whereas 76 cm in the horizontal and -19 cm in the vertical direction for the M_{JMA}7.3 earthquake. Compared with this report, our estimated results showed a good agreement.

6. CONCLUSIONS

In this research, the displacements of the GEONET Kumamoto station during the 2016 Kumamoto earthquake sequence were obtained by the relative positioning with the long baseline method. The relationship between the baseline distance and the positioning accuracy was examined using 113 GEONET stations with different distances between 50 km and 1,200 km. As the result of processing, the best positioning result was obtained when the master station was set in the range 200-400 km from the rover station. The fix ratios were more than 95% at all the points, and the standard deviations were also good compared with those from the stations with more than 400 km baseline distance.

Based on this result, the amount of crustal movement at the GEONET Kumamoto station caused by the Kumamoto earthquake was estimated and the obtained results were consistent with those released by the Geospatial Information Authority of Japan. We believe that the long baseline method can be used efficiently as an accurate relative GNSS positioning in the near future.

REFERENCES

Blewitt, G., 1989. Carrier Phase Ambiguity Resolution for the Global Positioning System Applied to Geodetic Baselines up to 2000 km, Journal of Geophysical Research, 94(B8), 10, pp. 187–203.

Boore, D., 2001. Effect of baseline corrections on displacement and response spectra for several recordings of the 1999 Chi-Chi, Taiwan, Earthquake, Bulleting of the Seismological Society of America, 91, pp. 1199-1211.

Brunini, C., Azpilicueta, F., 2010. GPS slant total electron content accuracy using the single layer model under different geomagnetic regions and ionospheric conditions, Journal of Geodesy, 84(5), pp. 293–304.

Ciraolo, L., Azpilicueta, F., Brunini, C., Meza, A., Radicella, S.M., 2007. Calibration errors on experimental slant total electron content (TEC) determined with GPS, Journal of Geodesy, 81(2), pp. 111–120.

Fujiwara, S., Yarai, H., Kobayashi, T., 2016. Small-displacement linear surface ruptures of the 2016 Kumamoto earthquake sequence detected by ALOS-2 SAR interferometry, Earth Planets Space, 68: 160, ISSN: 1880-5981.

Geospatial Information Authority of Japan, 2016. The 2016 Kumamoto Earthquake (in Japanese), http://www.gsi.go.jp/BOUSAI/H27-kumamoto-earthquake-index.html (accessed on 4 August 2017).

Karim, K.R., Yamazaki, F., 2002. Correlation of the JMA instrumental seismic intensity with strong motion parameters, Earthquake Engineering and Structural Dynamics, 31(5), pp. 1191-1212.

Kato, T., Terada, Y., Kinosita, M., Kakimoto, H., Issiki, H., Moriguchi, T., Takada, M., Tanno, T., Kanzaki, M., Johnson, I., 2001. A new tsunami monitoring system using RTK-GPS, Proceeding of ITS 2001, Session 5, Number 5-12, pp. 645-651.

Kawamoto S, Hiyama Y, Ohta Y, Nishimura T, 2016, First result from the GEONET real-time analysis system (REGARD): the case of the 2016 Kumamoto earthquakes, Earth Planets Space (2016) 68: 160, Online ISSN: 1880-5981.

Japan Meteorological Agency, 2017. The number of aftershocks of recent inland earthquakes in Japan, http://www.data.jma.go.jp/svd/eqev/data/2016_04_14_kumamoto/kaidan.pdf (accessed on 4 August 2017).

Liu, Z., 2010. A new automated cycle slip detection and repair method for a single dual-frequency GPS receiver, Journal of Geodesy, 85(3), pp 171-183

Milliken, R.J., Zoller, C.J., 1978. Principle of operation of NAVSTAR and system characteristics, Journal of the Institute of Navigation, 25(2), pp. 95-106.

Moya, L., Yamazaki, F., Liu, W., 2017a. Calculation of coseismic displacement from lidar data in the 2016 Kumamoto, Japan, earthquake, Natural Hazards and Earth System Science, 17, pp. 143–156.

Moya, L., Yamazaki, F., Liu, W., 2017b. Baseline effect on the estimation of crustal displacement using GPS kinematic relative positioning, 16th World Conference on Earthquake Engineering. Santiago, Chile, 11p.

Ohta, Y., Kobayashi, T., Tsushima, H., Miura, S., Hino, R., Takasu, T., Fujimoto, H., Iinuma, T., Tachibana, K., Demachi, T., Sato, T., Ohzono, M., Umino, N., 2012. Quasi real-time fault model estimation for near-field tsunami forecasting based on RTK-GPS analysis: Application to the 2011 Tohoku-Oki earthquake (Mw 9.0). Journal of Geophysical Research, 117, B02311, 16p.

Ronni, G., Michael, W., Jeffrey, F., 2017. The utility of GNSS for earthquake early warning in regions with sparse seismic networks, Bulletin of the Seismological Society of America, doi: 10.1785/0120160317.

Sagiya, T., 2004. A decade of GEONET: 1994-2003 The continuous GPS observation in Japan and its impact on earthquake studies. Earth Planets Space, 56, xxix-xli.

Shabestari, K.T., Yamazaki, F., 2001. A proposal of instrumental seismic intensity scale compatible with MMI evaluated from three-component acceleration records, Earthquake Spectra, 17(4), pp. 711-723.

Takasu, T., Yasuda, A., 2010. Kalman-filter-based integer ambiguity resolution strategy for long-baseline RTK with Ionosphere and Troposphere estimation, 23rd International Technical Meeting of the Satellite, Division Inst. of Nav., Portland, Oregon, 21–24 Sept.

Teunissen, P.J.G., 1995. The least-squares ambiguity decorrelation adjustment: a method for fast GPS integer ambiguity estimation, Journal of Geodesy, vol.70:65-82.

Teunissen, P.J.G., De Jonge, P.J., Tiberius, C.C.J.M., 1997. Performance of the LAMBDA method for fast GPS ambiguity resolution, Journal of the Institution of Navigation, 44(3), pp. 373–383.